

**The following resources related to this article are available online at [www.sciencemag.org](http://www.sciencemag.org) (this information is current as of October 27, 2009 ):**

**Updated information and services**, including high-resolution figures, can be found in the online version of this article at:

<http://www.sciencemag.org/cgi/content/full/323/5916/919>

**Supporting Online Material** can be found at:

<http://www.sciencemag.org/cgi/content/full/323/5916/919/DC1>

A list of selected additional articles on the Science Web sites **related to this article** can be found at:

<http://www.sciencemag.org/cgi/content/full/323/5916/919#related-content>

This article **cites 26 articles**, 5 of which can be accessed for free:

<http://www.sciencemag.org/cgi/content/full/323/5916/919#otherarticles>

This article has been **cited by** 5 article(s) on the ISI Web of Science.

This article appears in the following **subject collections**:

Physics

<http://www.sciencemag.org/cgi/collection/physics>

Information about obtaining **reprints** of this article or about obtaining **permission to reproduce this article** in whole or in part can be found at:

<http://www.sciencemag.org/about/permissions.dtl>

24. I. Fischer, N. Shah, A. Rosch, *Phys. Rev. B* **77**, 024415 (2008).  
 25. E. M. Forgan, E. P. Gibbons, K. A. McEwen, D. Fort, *Phys. Rev. Lett.* **62**, 470 (1989).  
 26. D. Gignoux, D. Schmitt, *J. Magn. Mater.* **100**, 99 (1991).  
 27. E. Grelet, *Phys. Rev. Lett.* **100**, 168301 (2008).  
 28. L. Brey, H. A. Fertig, R. Cote, A. H. MacDonald, *Phys. Rev. Lett.* **75**, 2562 (1995).  
 29. S. D. Bader, *Rev. Mod. Phys.* **78**, 1 (2006).  
 30. We thank A. N. Bogdanov, S. Dunsiger, E. M. Forgan, C. Franz, M. Garst, M. Janoschek, H. Kolb, M. Laver, S. Legl, T. Lorenz, W. Münzer, T. Nattermann, J. Peters, U. K. Rößler, B. Russ, R. Schwikowski, A. Vishwanath, M. Vojta, W. Zwerger, and the team of FRM II for discussions and support and K. von Bergmann for stimulating discussions and help in preparing Fig. 3C. We gratefully acknowledge financial support by SFB608 and the Alexander-von-Humboldt foundation.

## Supporting Online Material

www.sciencemag.org/cgi/content/full/323/5916/915/DC1

Materials and Methods

Figs. S1 to S6

References

3 October 2008; accepted 9 December 2008

10.1126/science.1166767

# Observation of Unconventional Quantum Spin Textures in Topological Insulators

D. Hsieh,<sup>1</sup> Y. Xia,<sup>1,2</sup> L. Wray,<sup>1,3</sup> D. Qian,<sup>1</sup> A. Pal,<sup>1</sup> J. H. Dil,<sup>4,5</sup> J. Osterwalder,<sup>5</sup> F. Meier,<sup>4,5</sup> G. Bihlmayer,<sup>6</sup> C. L. Kane,<sup>7</sup> Y. S. Hor,<sup>8</sup> R. J. Cava,<sup>8</sup> M. Z. Hasan<sup>1,2\*</sup>

A topologically ordered material is characterized by a rare quantum organization of electrons that evades the conventional spontaneously broken symmetry–based classification of condensed matter. Exotic spin-transport phenomena, such as the dissipationless quantum spin Hall effect, have been speculated to originate from a topological order whose identification requires a spin-sensitive measurement, which does not exist to this date in any system. Using Mott polarimetry, we probed the spin degrees of freedom and demonstrated that topological quantum numbers are completely determined from spin texture–imaging measurements. Applying this method to Sb and Bi<sub>1-x</sub>Sb<sub>x</sub>, we identified the origin of its topological order and unusual chiral properties. These results taken together constitute the first observation of surface electrons collectively carrying a topological quantum Berry’s phase and definite spin chirality, which are the key electronic properties component for realizing topological quantum computing bits with intrinsic spin Hall–like topological phenomena.

Ordered phases of matter such as a superfluid or a ferromagnet are usually associated with the breaking of a symmetry and are characterized by a local order parameter (*l*), and the typical experimental probes of these systems are sensitive to order parameters. The discovery of the quantum Hall effects in the 1980s revealed a new and rare type of order that is derived from an organized collective quantum motion of electrons (2–4). These so-called “topologically ordered phases” do not exhibit any symmetry-breaking and are characterized by a topological number (5) as opposed to a local order parameter. The classic experimental probe of topological quantum numbers is magneto-transport, in which measurements of the quantization of Hall conductivity  $\sigma_{xy} = ne^2/h$  (where *e* is the electric charge and *h* is Planck’s constant) reveals the value of

the topological number *n* that characterizes the quantum Hall effect state (6).

Recent theoretical and experimental studies suggest that a new class of quantum Hall–like topological phases can exist in spin-orbit materials without external magnetic fields, with interest centering on two examples: the “quantum spin Hall insulator” (7–9) and the “strong topological insulator” (10, 11). Their topological order is believed to give rise to unconventional spin physics at the sample edges or surfaces, with potential applications ranging from dissipationless spin currents (12) to topological (fault-tolerant) quantum computing (13). However, unlike conventional quantum Hall systems, these previously unmeasured topological phases do not necessarily exhibit a quantized charge or spin response ( $\sigma_{xy} \neq ne^2/h$ ) (14, 15). In fact, the spin polarization is not a conserved quantity in a spin-orbit material. Thus, their topological quantum numbers, the analogs of *n*, cannot be measured via the classic von Klitzing–type (2) transport methods.

Here we show that spin-resolved angle-resolved photoemission spectroscopy (spin-ARPES) can perform analogous measurements for topological insulators and quantum spin Hall materials. We measured all of the topological numbers for Bi<sub>1-x</sub>Sb<sub>x</sub> and provide an identification of its spin texture, which heretofore was unmeasured despite its surface states (SSs) having been observed (10). The measured spin texture reveals the existence

of a nonzero geometrical quantum phase [Berry’s phase (16, 17)] and the handedness or chiral properties. More importantly, this technique enables us to investigate aspects of the metallic regime of the Bi<sub>1-x</sub>Sb<sub>x</sub> series, such as spin properties in pure Sb, which are necessary to determine the microscopic origin of topological order. Our measurements on pure metallic Sb show that its surface carries a  $\pi$  geometrical (Berry’s) phase and chirality property unlike the conventional spin-orbit metals such as gold (Au), which has zero net Berry’s phase and no topological chirality (18).

Strong topological materials are distinguished from ordinary materials such as Au by a topological quantum number  $\nu_0 = 1$  or 0, respectively (14, 15). For Bi<sub>1-x</sub>Sb<sub>x</sub>, theory has shown that  $\nu_0$  is determined solely by the character of the bulk electronic wave functions at the *L* point in the three-dimensional (3D) Brillouin zone (BZ). When the lowest energy-conduction band state consists of an antisymmetric combination of atomic p-type orbitals (*L<sub>a</sub>*) and the highest energy valence band state consists of a symmetric combination (*L<sub>s</sub>*), then  $\nu_0 = 1$ , and vice versa for  $\nu_0 = 0$  (11). Although the bonding nature (parity) of the states at *L* is not revealed in a measurement of the bulk band structure, the value of  $\nu_0$  can be determined from the spin textures of the surface bands that form when the bulk is terminated. In particular, a  $\nu_0 = 1$  topology requires the terminated surface to have a Fermi surface (FS) (11) that supports a nonzero Berry’s phase (an odd as opposed to an even multiple of  $\pi$ ), which is not realizable in an ordinary spin-orbit material.

In a general inversion symmetric spin-orbit insulator, the bulk states are spin-degenerate because of a combination of space-inversion symmetry [ $E(\vec{k}, \uparrow) = E(-\vec{k}, \uparrow)$ ] and time-reversal symmetry [ $E(\vec{k}, \uparrow) = E(-\vec{k}, \downarrow)$ ], where *E* is the energy and  $\vec{k}$  is the electron momentum. Because space-inversion symmetry is broken at the terminated surface, the spin degeneracy of surface bands can be lifted by the spin-orbit interaction (19–21). However, according to Kramers theorem (16), they must remain spin-degenerate at four special time-reversal invariant momenta ( $\vec{k}_T = \bar{\Gamma}, \bar{M}$ ) in the surface BZ (11), which for the (111) surface of Bi<sub>1-x</sub>Sb<sub>x</sub> are located at  $\bar{\Gamma}$  and three equivalent  $\bar{M}$  points (Fig. 1A).

Depending on whether  $\nu_0$  equals 0 or 1, the FS pockets formed by the surface bands will enclose the four  $\vec{k}_T$  an even or odd number of times, respectively. If a FS pocket does not enclose  $\vec{k}_T$  ( $= \bar{\Gamma}, \bar{M}$ ), it is irrelevant for the topology (11, 20). Because the wave function of a single electron spin acquires a geometric phase

<sup>1</sup>Joseph Henry Laboratories of Physics, Department of Physics, Princeton University, Princeton, NJ 08544, USA. <sup>2</sup>Princeton Center for Complex Materials, Princeton Institute for the Science and Technology of Materials, Princeton University, Princeton, NJ 08544, USA. <sup>3</sup>Advanced Light Source, Lawrence Berkeley National Laboratory, Berkeley, CA 94305, USA. <sup>4</sup>Swiss Light Source, Paul Scherrer Institute, CH-5232 Villigen, Switzerland. <sup>5</sup>Physik-Institut, Universität Zürich-Irchel, 8057 Zürich, Switzerland. <sup>6</sup>Institut für Festkörperforschung, Forschungszentrum Jülich, D-52425 Jülich, Germany. <sup>7</sup>Department of Physics and Astronomy, University of Pennsylvania, Philadelphia, PA 19104, USA. <sup>8</sup>Department of Chemistry, Princeton University, Princeton, NJ 08544, USA.

\*To whom correspondence should be addressed. E-mail: mzhazan@princeton.edu

factor of  $\pi$  (16) because it evolves by  $360^\circ$  in momentum space along a Fermi contour enclosing a  $\vec{k}_T$ , an odd number of Fermi pockets enclosing  $\vec{k}_T$  in total implies a  $\pi$  geometrical (Berry's) phase (11). In order to realize a  $\pi$  Berry's phase, the surface bands must be spin-polarized and exhibit a partner-switching (11) dispersion behavior between a pair of  $\vec{k}_T$ . This means that any pair of spin-polarized surface bands that are degenerate at  $\bar{\Gamma}$  must not reconnect at  $\bar{M}$  or must separately connect to the bulk valence and conduction band in between  $\bar{\Gamma}$  and  $\bar{M}$ . The partner-switching behavior is realized in Fig. 1C because the spin-down band connects to and is degenerate with different spin-up bands at  $\bar{\Gamma}$  and  $\bar{M}$ . The partner-switching behavior is realized in Fig. 2A because the spin-up and spin-down bands emerging from  $\bar{\Gamma}$  separately merge into the bulk valence and conduction bands, respectively, between  $\bar{\Gamma}$  and  $\bar{M}$ .

We first investigated the spin properties of the topological insulator phase. Spin-integrated ARPES (19) intensity maps of the (111) SSs of insulating  $\text{Bi}_{1-x}\text{Sb}_x$  taken at the Fermi level ( $E_F$ ) (Fig. 1, D and E) show that a hexagonal FS encloses  $\bar{\Gamma}$ , whereas dumbbell-shaped FS pockets that are much weaker in intensity enclose  $\bar{M}$ . By examining the surface-band dispersion below the Fermi level (Fig. 1F), it is clear that the central hexagonal FS is formed by a single band (Fermi crossing 1), whereas the dumbbell-shaped FSs are formed by the merger of two bands (Fermi crossings 4 and 5) (10).

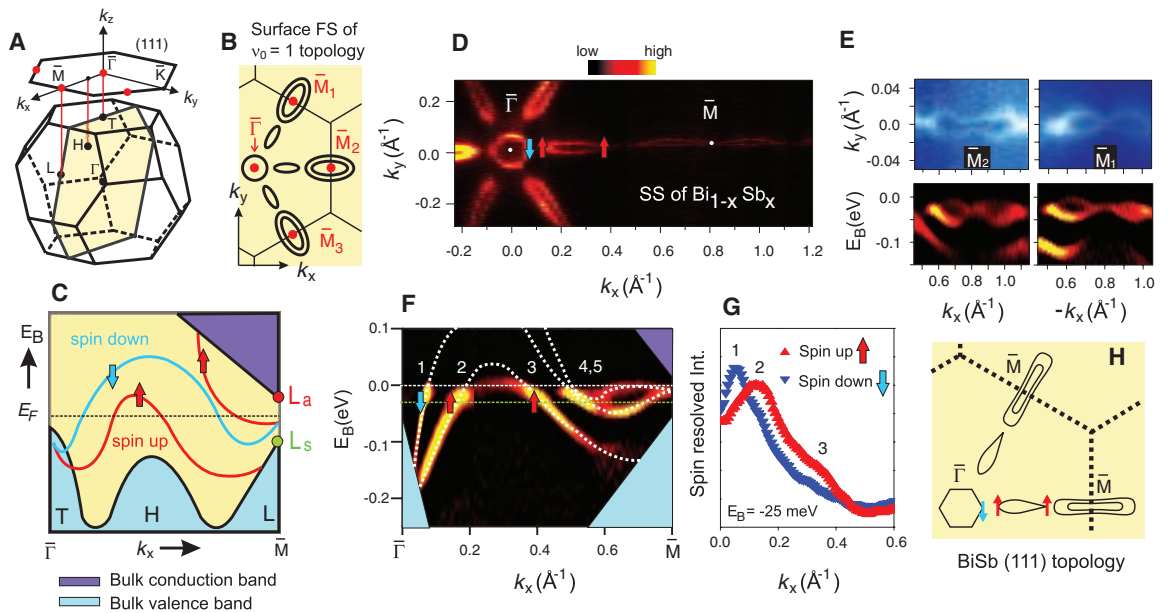
This band dispersion resembles the partner-switching dispersion behavior characteristic of topological insulators. To check this scenario and determine the topological index  $\nu_0$ , we have carried out spin-resolved photoemission spectroscopy. Figure 1G shows a spin-resolved momentum distribution curve taken along the  $\bar{\Gamma}-\bar{M}$  direction at a binding energy  $E_B = -25$  meV (Fig. 1G). The data reveal a clear difference between the spin-up and spin-down intensities of bands 1, 2, and 3 and show that bands 1 and 2 have opposite spin whereas bands 2 and 3 have the same spin. The former observation confirms that bands 1 and 2 form a spin-orbit split pair, and the latter observation suggests that bands 2 and 3 (as opposed to bands 1 and 3) are connected above the Fermi level and form one band. This is further confirmed by directly imaging the bands through raising the chemical potential via doping [supporting online material (SOM) text] (22). Irrelevance of bands 2 and 3 to the topology is consistent with the fact that the FS pocket they form does not enclose any  $\vec{k}_T$ . Because of a dramatic intrinsic weakening of signal intensity near crossings 4 and 5, and the small energy and momentum splittings of bands 4 and 5 lying at the resolution limit of modern spin-ARPES spectrometers, no conclusive spin information about these two bands can be drawn from the methods employed in obtaining the data sets in Fig. 1, G and H. However, whether bands 4 and 5 are both singly or doubly degenerate does not change the fact

that an odd number of spin-polarized FSs enclose the  $\vec{k}_T$ , which provides evidence that  $\text{Bi}_{1-x}\text{Sb}_x$  has  $\nu_0 = 1$  and that its surface supports a non-trivial Berry's phase of topological origin.

We investigated the quantum origin of topological order in this class of materials. It has been theoretically speculated that the novel topological order originates from the parities of the electrons in pure Sb (11, 23). The origin of the topological effects can only be tested by measuring the spin texture of the Sb surface (20), which has not been measured. Based on quantum oscillation and magneto-optical studies, the bulk band structure of Sb is known to evolve from that of insulating  $\text{Bi}_{1-x}\text{Sb}_x$  through the holelike band at  $H$  rising above  $E_F$  and the electron-like band at  $L$  sinking below  $E_F$  (23). The relative energy ordering of the  $L_a$  and  $L_s$  states in Sb again determines whether the SS pair emerging from  $\bar{\Gamma}$  switches partners (Fig. 2A) or not (Fig. 2B) between  $\bar{\Gamma}$  and  $\bar{M}$ , and in turn determines whether they support a nonzero Berry's phase.

In a conventional spin-orbit metal such as Au, a free-electron-like SS is split into two parabolic spin-polarized sub-bands that are shifted in  $\vec{k}$ -space relative to each other (18). Two concentric spin-polarized FSs are created, one having an opposite sense of in-plane spin rotation from the other, that enclose  $\bar{\Gamma}$ . Such a FS arrangement, like the schematic shown in Fig. 2B, does not support a nonzero Berry's phase because the  $\vec{k}_T$  are enclosed an even number of times (two times for most known materials).

**Fig. 1.** Spin spectrum of a topological insulator and spin-resolved spectroscopy results. (A) Schematic sketches of the bulk BZ and (111) surface BZ of the  $\text{Bi}_{1-x}\text{Sb}_x$  crystal series. The high symmetry points ( $L$ ,  $H$ ,  $T$ ,  $\Gamma$ ,  $\bar{\Gamma}$ ,  $\bar{M}$ ,  $\bar{K}$ ) are identified. (B) Schematic of FS pockets formed by the SSs of a topological insulator that carries a  $\pi$  Berry's phase. (C) Partner-switching band structure topology: schematic of spin-polarized SS dispersion and connectivity between  $\bar{\Gamma}$  and  $\bar{M}$  required to realize the FS pockets shown in (B).  $L_a$  and  $L_s$  label bulk states at  $L$  that are antisymmetric and symmetric, respectively, under a parity transformation. (D) Spin-integrated ARPES intensity map of the SS of  $\text{Bi}_{0.91}\text{Sb}_{0.09}$  at  $E_F$ . Arrows point in the measured direction of the spin. (E) High-resolution ARPES intensity map of the SS at  $E_F$  that enclose the  $\bar{M}_1$  and  $\bar{M}_2$  points. Corresponding band dispersion (second derivative images) are shown below. The left-right asymmetry of the band dispersions are due to the slight offset of the alignment from the  $\bar{\Gamma}-\bar{M}_1$  ( $\bar{M}_2$ ) direction. (F) Surface band-dispersion image along the  $\bar{\Gamma}-\bar{M}$  direction showing five Fermi-level crossings. The intensity of bands 4 and 5 is



scaled up for clarity (the dashed white lines are guides to the eye). The schematic projection of the bulk valence and conduction bands are shown in shaded blue and purple areas. (G) Spin-resolved momentum distribution curves presented at  $E_B = -25$  meV showing single-spin degeneracy of bands at 1, 2, and 3. Spin up and down correspond to spin pointing along the  $+\hat{y}$  and  $-\hat{y}$  direction, respectively. (H) Schematic of the spin-polarized surface FS observed in our experiments. It is consistent with a  $\nu_0 = 1$  topology [compare (B) and (H)].

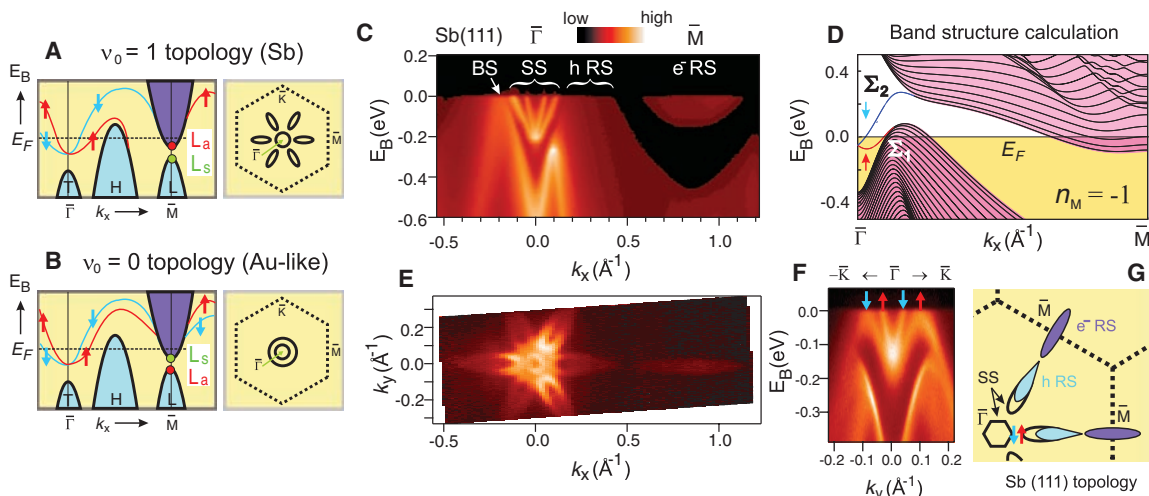
However, for Sb, this is not the case. Figure 2C shows a spin-integrated ARPES intensity map of Sb(111) from  $\bar{\Gamma}$  to  $\bar{M}$ . By performing a systematic incident photon energy–dependence study of such spectra, previously unavailable with He lamp sources (24), it is possible to identify two V-shaped SSs centered at  $\bar{\Gamma}$ , a bulk state located near  $k_x = -0.25 \text{ \AA}^{-1}$  and resonance states centered about  $k_x = 0.25 \text{ \AA}^{-1}$  and  $\bar{M}$  that are hybrid states formed by surface and bulk states (SOM text) (19, 22). An examination of the ARPES intensity map of the Sb(111) surface and resonance states at  $E_F$  (Fig. 2E) reveals that the central surface FS enclosing  $\bar{\Gamma}$  is formed only by the inner V-shaped SS. The outer V-shaped SS, however, forms part of a teardrop-shaped FS that does not enclose  $\bar{\Gamma}$ , unlike the case in Au. This teardrop-shaped FS is formed partly by the outer V-shaped SS and partly by the holelike resonance state. The electron-like resonance state FS enclosing  $\bar{M}$  does not affect the determination of  $\nu_0$  because it must be doubly spin-degenerate (SOM text) (22). Such a FS geometry (Fig. 2G) suggests that the V-shaped SS pair may undergo a partner-switching behavior as expected in Fig. 2A. This behavior is most clearly seen in a cut taken along the  $\bar{\Gamma} - \bar{K}$  direction because the top of the bulk valence band is well below  $E_F$  (Fig. 2F), showing only the inner V-shaped SS crossing  $E_F$  whereas the outer V-shaped SS bends back toward the bulk valence band near  $k_x = 0.1 \text{ \AA}^{-1}$  before reaching  $E_F$ . The additional support for this band-dispersion behavior comes from tight binding-surface calculations on Sb (Fig. 2D), which closely match with experimental data below  $E_F$ . Our observation of a single-surface band forming a FS enclosing  $\bar{\Gamma}$  suggests that pure Sb is probably described by  $\nu_0 = 1$  and that its surface may support a Berry's phase.

**Fig. 2.** Topological character of pure Sb revealed on the (111) SSs. Schematic of the bulk-band structure (shaded areas) and surface-band structure (red and blue lines) of Sb near  $E_F$  for a (A) topologically nontrivial and (B) topologically trivial (Au-like) case, together with their corresponding surface FSs are shown. (C) Spin-integrated ARPES spectrum of Sb(111) along the  $\bar{\Gamma} - \bar{M}$  direction. The surface states are denoted by SS, bulk states by BS, and the holelike resonance states and electron-like resonance states by hRS and e<sup>-</sup>RS, respectively. (D) Calculated SS band structure of Sb(111) based on the methods in (20, 30). The continuum bulk-energy bands are represented with pink-shaded regions, and the lines show the discrete bands of a 100-layer slab. The red and blue single bands, denoted  $\Sigma_1$  and  $\Sigma_2$ , are the SS bands with spin polarization  $\langle \hat{P} \rangle \propto +\hat{y}$  and  $\langle \hat{P} \rangle \propto -\hat{y}$ , respectively. (E) ARPES intensity map of Sb(111) at  $E_F$  in the  $k_x$ - $k_y$  plane. The only one FS encircling  $\bar{\Gamma}$  seen in the data is formed by the inner V-shaped SS band seen in (C) and (F). The outer V-shaped band bends back

Confirmation of a surface  $\pi$  Berry's phase rests critically on a measurement of the relative spin orientations (up or down) of the SS bands near  $\bar{\Gamma}$  so that the partner switching is indeed realized, which cannot be done without spin resolution. We achieved spin resolution by using a Mott polarimeter that measures two orthogonal spin components of a photoemitted electron (25, 26). These two components are along the  $y'$  and  $z'$  directions of the Mott coordinate frame, which lie predominantly in and out of the sample (111) plane respectively. Each of these two directions represents a normal to a scattering plane defined by the photoelectron incidence direction on a Au foil and two electron detectors mounted on either side (left and right) (Fig. 3A). Strong spin-orbit coupling of atomic Au is known to create an asymmetry in the scattering of a photoelectron off the Au foil that depends on its spin component normal to the scattering plane (26). This leads to an asymmetry  $A_{y',z'}$  between the left intensity ( $I_{y',z'}^L$ ) and right intensity ( $I_{y',z'}^R$ ) given by  $A_{y',z'} = [(I_{y',z'}^L - I_{y',z'}^R)/(I_{y',z'}^L + I_{y',z'}^R)]$ , which is related to the spin polarization  $P_{y',z'} = (1/S_{\text{eff}}) \times A_{y',z'}$  through the Sherman function  $S_{\text{eff}} = 0.085$  (25, 26). Spin-resolved momentum-distribution curve data sets of the SS bands along the  $-\bar{M} - \bar{\Gamma} - \bar{M}$  cut at  $E_B = -30 \text{ meV}$  (Fig. 3B) are shown for maximal intensity. Figure 3D displays both  $y'$  and  $z'$  polarization components along this cut, showing clear evidence that the bands are spin polarized with spins pointing largely in the (111) plane. In order to estimate the full 3D spin-polarization vectors from a two-component measurement (which is not required to prove the topological partner switching or the Berry's phase), we fit a model polarization curve (27), which takes the polarization directions associated with each momentum-

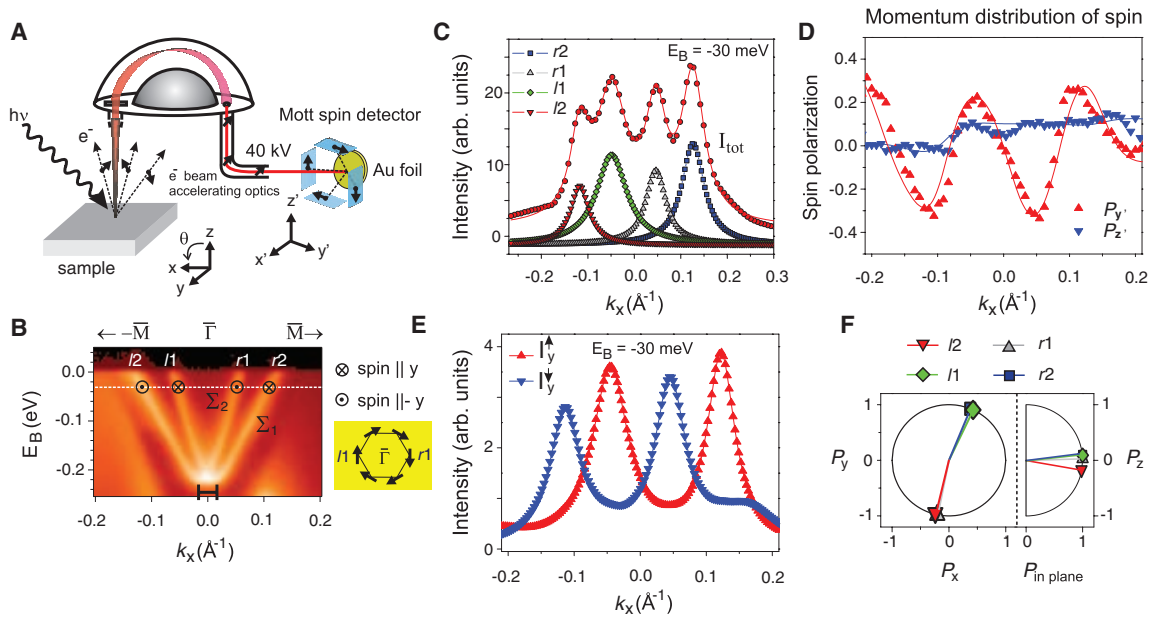
distribution curve peak (Fig. 3C) as input parameters, with the constraint that each polarization vector has length one (in angular momentum units of  $\hbar/2$ ,  $\hbar$  being  $h$  divided by  $2\pi$ ). Our fitted polarization vectors are displayed in the sample ( $x, y, z$ ) coordinate frame (Fig. 3F), from which we derived the spin-resolved momentum distribution curves for the spin components parallel ( $I_y^{\uparrow}$ ) and anti-parallel ( $I_y^{\downarrow}$ ) to the  $y$  direction as shown in Fig. 3E (SOM text) (22). There is a clear difference in  $I_y^{\uparrow}$  and  $I_y^{\downarrow}$  at each of the four momentum-distribution curve peaks, indicating that the SS bands are spin-polarized (Fig. 3E), which is possible to conclude even without a full 3D fitting. Each of the pairs  $l2/l1$  and  $r1/r2$  have opposite spin, which is consistent with the behavior of a spin-split pair, and the spin polarization of these bands is reversed on either side of  $\bar{\Gamma}$  in accordance with the system being time-reversal symmetric [ $E(\vec{k}, \uparrow) = E(-\vec{k}, \downarrow)$ ] (Fig. 3F). The measured spin texture of the Sb(111) SSs (Fig. 3), together with the connectivity of the surface bands (Fig. 2), distinctively determines its belonging to the  $\nu_0 = 1$  class. Therefore, the surface of Sb carries a nonzero ( $\pi$ ) Berry's phase via the inner V-shaped band, and pure Sb can be regarded as the parent matrix of the  $\text{Bi}_{1-x}\text{Sb}_x$  topological insulator class; the topological order originates from the parity set of Sb wave functions.

Our spin-polarized measurement methods (Figs. 1 and 3) uncover a new type of topological quantum number  $n_M$  that provides information about the chirality properties. Topological theory suggests that the bulk electronic states in the mirror ( $k_y = 0$ ) plane can be classified in terms of a number  $n_M$  ( $= \pm 1$ ) that describes the handedness (either left- or right-handed) or chirality of the surface spins that can be directly measured or seen



toward the bulk band that is best seen in data in (F). (F) ARPES spectrum of Sb(111) along the  $\bar{\Gamma} - \bar{K}$  direction shows that the outer V-shaped SS band merges with the bulk band. (G) Schematic of the surface FS of Sb(111) showing the pockets formed by the SSs (unfilled) and the resonance states (blue and purple). The purely SS Fermi pocket encloses only one  $\bar{k}_T$ , namely  $\bar{\Gamma} (= \bar{k}_T)$ , and is therefore consistent with the  $\nu_0 = 1$  topological classification of Sb, which is different from Au [compare (B) and (G)]. As discussed in the text, the hRS and e<sup>-</sup>RS count trivially.

**Fig. 3.** Spin texture of topological surface-edge states and chirality. **(A)** Experimental geometry of the spin-ARPES study. At normal emission ( $\theta = 0^\circ$ ), the sensitive  $y'$  axis of the Mott detector is rotated by  $45^\circ$  from the sample  $\bar{\Gamma}$  to  $-\bar{M}$  ( $\parallel -\hat{x}$ ) direction, and the sensitive  $z'$  axis of the Mott detector is parallel to the sample normal ( $\parallel \hat{z}$ ). **(B)** Spin-integrated ARPES spectrum of Sb(111) along the  $-\bar{M}-\bar{\Gamma}-\bar{M}$  direction. The momentum splitting between the band minima is indicated by the black bar and is approximately  $0.03 \text{ \AA}^{-1}$ . A schematic of the spin chirality of the central FS based on the spin-ARPES results is shown on the right. **(C)** Momentum-distribution curve of the spin-averaged spectrum at  $E_B = -30 \text{ meV}$  [shown in (B) by white line] together with the Lorentzian peaks of the fit. **(D)** Measured spin-polarization curves (red and blue triangles) for the detector  $y'$  and  $z'$  components together with the fitted lines by using the two-step fitting routine (27). **(E)** Spin-resolved spectra for the sample  $y$  component based on the fitted spin-polarization curves shown in (D).



Up triangles represent a spin direction along the  $+\hat{y}$  direction, and down triangles represent a spin direction along the  $-\hat{y}$  direction. **(F)** The in-plane and out-of-plane spin polarization components in the sample coordinate frame obtained from the spin-polarization fit. Overall spin-resolved data and the fact that the surface band that forms the central electron pocket ( $\vec{P}$ )  $\propto -\hat{y}$  along the  $+k_x$  direction, as in (E), suggest a left-handed chirality [schematic in (B)].

in spin-resolved experiments (20). We next determined the value of  $n_M$  from our data: From Fig. 1, it is seen that a single- (one-) surface band, which switches partners at  $\bar{M}$ , connects the bulk valence and conduction bands, so  $|n_M| = 1$  (SOM text) (22). The sign of  $n_M$  is related to the direction of the spin polarization ( $\vec{P}$ ) of this band (20), which is constrained by mirror symmetry to point along  $\pm \hat{y}$ . Because the central electron-like FS enclosing  $\bar{\Gamma}$  intersects six mirror invariant points (Fig. 3B), the sign of  $n_M$  distinguishes two distinct types of handedness for this spin-polarized FS. Figures 1F and 3 show that for both  $\text{Bi}_{1-x}\text{Sb}_x$  and Sb, the surface band that forms this electron pocket has  $\langle \vec{P} \rangle \propto -\hat{y}$  along the  $k_x$  direction, which suggests a left-handed rotation sense for the spins around this central FS and thus  $n_M = -1$ . Therefore, both insulating  $\text{Bi}_{1-x}\text{Sb}_x$  and pure Sb possess equivalent chirality properties: a definite spin-rotation sense (left-handed chirality) (Fig. 3B) and a topological Berry's phase.

These spin-resolved experimental measurements reveal an intimate and straightforward connection between the topological numbers ( $\nu_0, n_M$ ) and the physical observables. Although  $\nu_0$  determines whether the surface electrons support a nontrivial Berry's phase, if they do, the  $n_M$  determines the spin-handedness of the FS that manifests this Berry's phase. The 2D topological Berry's phase is a critical signature of group  $Z_2$  topological order and is not realizable in isolated 2D electron systems nor on the surfaces of conventional spin-orbit or exchange-coupled magnetic materials. A nonzero Berry's

phase is known, theoretically, to protect an electron system against the almost universal weak-localization behavior in their low-temperature transport (11, 13) and is expected to form the key element for fault-tolerant quantum computation schemes (13, 28, 29). Its remarkable realization on the  $\text{Bi}_{1-x}\text{Sb}_x$  surface represents an unprecedented example of a 2D  $\pi$  Berry's phase and opens the possibility for building realistic prototype systems to test quantum computing modules. In general, our results demonstrate that spin-ARPES is a powerful probe of topological order and quantum spin Hall physics, which opens up a new search front for topological materials for novel spin devices and fault-tolerant quantum computing.

#### References and Notes

- N. W. Ashcroft, N. D. Mermin, *Solid State Physics* (Holt, Rinehart and Winston, NY, 1976).
- K. von Klitzing, G. Dorda, M. Pepper, *Phys. Rev. Lett.* **45**, 494 (1980).
- R. B. Laughlin, *Phys. Rev. Lett.* **50**, 1395 (1983).
- X.-G. Wen, *Int. J. Mod. Phys. B* **4**, 239 (1990).
- D. J. Thouless *et al.*, *Phys. Rev. Lett.* **49**, 405 (1982).
- J. E. Avron, D. Osadchy, R. Seiler, *Phys. Today* **56**, 38 (2003).
- M. König *et al.*, *Science* **318**, 766 (2007).
- B. A. Bernevig, T. L. Hughes, S.-C. Zhang, *Science* **314**, 1757 (2006).
- N. Nagaoa, *Science* **318**, 758 (2007).
- D. Hsieh *et al.*, *Nature* **452**, 970 (2008).
- L. Fu, C. L. Kane, *Phys. Rev. B* **76**, 045302 (2007).
- X.-L. Qi, T. Hughes, S.-C. Zhang, *Phys. Rev. B* **78**, 195424 (2008).
- L. Fu, C. L. Kane, *Phys. Rev. Lett.* **100**, 096407 (2008).
- C. L. Kane, E. J. Mele, *Phys. Rev. Lett.* **95**, 146802 (2005).
- J. E. Moore, L. Balents, *Phys. Rev. B* **75**, 121306 (2007).
- J. J. Sakurai, *Modern Quantum Mechanics* (Addison-Wesley, NY, 1994).

- M. V. Berry, *Proc. R. Soc. London Ser. A* **392**, 45 (1984).
- M. Hoesch *et al.*, *Phys. Rev. B* **69**, 241401 (2004).
- S. Hufner, *Photoelectron Spectroscopy* (Springer-Verlag, Berlin, 1995).
- J. C. Y. Teo, L. Fu, C. L. Kane, *Phys. Rev. B* **78**, 045426 (2008).
- T. Hirahara *et al.*, *Phys. Rev. B* **76**, 153305 (2007).
- Materials and methods, including details of sample characterization, data analysis, and theoretical background, are available as supporting material on Science Online.
- B. Lenoir *et al.*, *Int. Conf. Thermoelec.* **15**, 1 (1996).
- K. Sugawara *et al.*, *Phys. Rev. Lett.* **96**, 046411 (2006).
- M. Hoesch *et al.*, *J. Electron Spectrosc. Relat. Phenom.* **124**, 263 (2002).
- T. J. Gay, F. B. Dunning, *Rev. Sci. Instrum.* **63**, 1635 (1992).
- F. Meier *et al.*, *Phys. Rev. B* **77**, 165431 (2008).
- P. J. Leek *et al.*, *Science* **318**, 1889 (2007).
- A. Kitaev, *Ann. Phys. (NY)* **303**, 2 (2003).
- Y. Liu, E. Allen, *Phys. Rev. B* **52**, 1566 (1995).
- We thank J. Teo for providing the SS band calculations of antimony (Sb); A. Fedorov, L. Patthey, and D.-H. Lu for beamline assistance; and D. Haldane, B. I. Halperin, N. P. Ong, D. A. Huse, F. Wilczek, P. W. Anderson, D. C. Tsui, J. E. Moore, L. Fu, L. Balents, D.-H. Lee, S. Sachdev, P. A. Lee, and X.-G. Wen for stimulating discussions. C.L.K. was supported by NSF grant DMR-0605066. The spin-resolved ARPES experiments are supported by NSF through the Center for Complex Materials (DMR-0819860) and Princeton University; the use of synchrotron X-ray facilities (ALS-LBNL, Berkeley, and SSRF-SLAC, Stanford) is supported by the Basic Energy Sciences of the U.S. Department of Energy (DE-FG-02-05ER46200) and by the Swiss Light Source, Paul Scherrer Institute, Villigen, Switzerland.

#### Supporting Online Material

www.sciencemag.org/cgi/content/full/323/5916/919/DC1  
Materials and Methods  
SOM Text  
Figs. S1 to S6  
References

27 October 2008; accepted 7 January 2009  
10.1126/science.1167733